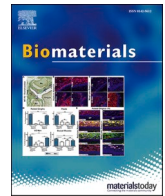| Title	Human iPS cell-derived cartilaginous tissue spatially and functionally replaces nucleus pulposus
Author(s)	Kamatani, Takashi; Hagizawa, Hiroki; Yarimitsu, Seido et al.
Citation	Biomaterials. 2022, 284, p. 121491
Version Type	VoR
URL	https://hdl.handle.net/11094/93297
rights	This article is licensed under a Creative Commons Attribution 4.0 International License.
Note	

Human iPS cell-derived cartilaginous tissue spatially and functionally replaces nucleus pulposus

Takashi Kamatani [a,b,1], Hiroki Hagizawa [a,b,g,1], Seido Yarimitsu [c], Miho Morioka [a,g], Saeko Koyamatsu [a,g], Michihiko Sugimoto [d], Joe Kodama [b], Junko Yamane [e], Hiroyuki Ishiguro [b], Shigeyuki Shichino [f], Kuniya Abe [d], Wataru Fujibuchi [e], Hiromichi Fujie [c], Takashi Kaito [b], Noriyuki Tsumaki [a,g,*]

[a] Department of Clinical Application, Center for iPS Cell Research and Application, Kyoto University, 53 Kawahara-cho, Shogoin, Sakyo-ku, Kyoto, 606-8507, Japan
[b] Department of Orthopaedic Surgery, Graduate School of Medicine, Osaka University, 2-2 Yamadaoka, Suita, Osaka, 565-0871, Japan
[c] Department of Mechanical Systems Engineering, Faculty of Systems Design, Tokyo Metropolitan University, 1-1 Minami-Osawa, Hachioji, Tokyo, 192-0397, Japan
[d] Technology and Development Team for Mammalian Genome Dynamics, RIKEN BioResource Research Center, 3-1-1 Koyadai, Tsukuba, Ibaraki, 305-0074, Japan
[e] Department of Life Science Frontiers, Center for iPS Cell Research and Application, Kyoto University, 53 Kawahara-cho, Shogoin, Sakyo-ku, Kyoto, 606-8507, Japan
[f] Division of Molecular Regulation of Inflammatory and Immune Diseases, Research Institute of Biomedical Sciences, Tokyo University of Science, Building 17 Second Floor, 2641, Yamasaki, Noda, Chiba, 278-0042, Japan
[g] Department of Tissue Biochemistry, Graduate School of Medicine and Frontier Biosciences, Osaka University, 2-2 Yamadaoka, Suita, Osaka, 565-0871, Japan

ARTICLE INFO

ABSTRACT

The loss of nucleus pulposus (NP) precedes the intervertebral disk (IVD) degeneration that causes back pain. Here, we demonstrate that the implantation of human iPS cell-derived cartilaginous tissue (hiPS-Cart) restores this loss by replacing lost NP spatially and functionally. NP cells consist of notochordal NP cells and chondrocyte-like NP cells. Single cell RNA sequencing (scRNA-seq) analysis revealed that cells in hiPS-Cart corresponded to chondrocyte-like NP cells but not to notochordal NP cells. The implantation of hiPS-Cart into a nuclectomized space of IVD in nude rats prevented the degeneration of the IVD and preserved its mechanical properties. hiPS-Cart survived and occupied the nuclectomized space for at least six months after implantation, indicating spatial and functional replacement of lost NP by hiPS-Cart. Further scRNA-seq analysis revealed that hiPS-Cart cells changed their profile after implantation, differentiating into two lineages that are metabolically distinct from each other. However, post-implanted hiPS-Cart cells corresponded to chondrocyte-like NP cells only and did not develop into notochordal NP cells, suggesting that chondrocyte-like NP cells are nearly sufficient for NP function. The data collectively indicate that hiPS-Cart is a candidate implant for regenerating NP spatially and functionally and preventing IVD degeneration.

1. Introduction

Low back pain is a leading cause of disabilities throughout the world and engenders a tremendous socioeconomic burden [1,2]. It has been estimated that intervertebral disk (IVD) degeneration accounts for 22–42% of patients with low back pain [3,4]. IVD degeneration frequently leads to more debilitating conditions, such as lumbar disk herniation, lumbar spinal stenosis, and spinal deformity, which are collectively called degenerative disk diseases [5–7]. Conservative treatments for IVD degeneration may alleviate the symptoms but do not restore the degenerated IVD to its healthy state. Surgical interventions, such as decompression, fusion, and deformity correction surgeries, are palliative, do not resolve the pathology, and are associated with complications, including adjacent segment disease and implant failure, that commonly require revision surgery [8,9]. Moreover, because IVD degeneration is an irreversible condition, there is a need for regenerative treatments.

Anatomically, IVDs reside between vertebral bodies and constitute

---

the spinal column. Functionally, IVDs resist the axial compression load of the spine and provide flexibility of the spinal column. This mechanical function is conferred by the anatomical structure of the IVD, in which nucleus pulposus (NP) in the center is surrounded by annulus fibrosus (AF) in the periphery. NP is viscoelastic and avascular and is composed of NP cells and extracellular matrix (ECM), which is produced and maintained by the NP cells. The ECM determines the mechanical properties of the NP. The ECM also provides NP cells with an environment necessary for the homeostasis of NP cells.

Although the exact origin of IVD degeneration has not been determined, NP is believed to be the place of onset [10,11], suggesting it should be targeted by regenerative treatment to restore the IVD. At the early stage, biomolecular therapy, such as recombinant proteins and genes, facilitates the production of the ECM if abundant and viable cells exist in NP. The implantation of diskogenic cells is also expected to secrete anabolic factors that facilitate the production of the ECM from native viable cells through trophic effects. At advanced stages, however, when both NP cells and the ECM are lost, the implantation of diskogenic cells alone cannot regenerate NP, because the cells do not maintain the characters of NP cells in the absence of NP-ECM. Thus, the ultimate goal for regenerative treatment includes developing a tissue-engineered NP construct containing both viable cells and NP-ECM that is implanted into the NP space and replaces NP to restore the biomechanical function [12].

NP-ECM consists of collagen fibrils that form three-dimensional (3D) networks providing scaffolding for proteoglycans [13,14]. Proteoglycans consists of the core protein that links abundant glycosaminoglycans. Interestingly, this specific ECM composition in NP is shared with cartilage. Articular cartilage (AC) has specific viscoelasticity and covers the ends of bones to resist compression load and provide lubrication in diarthrodial joints. In both NP-ECM and AC-ECM, collagen fibrils are composed of types II, IX and XI collagen molecules and the proteoglycan core protein is aggrecan. The composition ratio of proteoglycan to collagen content in NP-ECM is higher than that in AC-ECM, which assumingly explains the different properties needed for the specific mechanical functions of NP and AC.

Induced pluripotent stem cells (iPSCs) are reprogrammed somatic cells that have the same function as embryonic stem cells (ESCs) but without the ethical issues involving embryo destruction [15]. Thus, iPSCs are a promising cell source for regenerative therapy due to their unlimited proliferative and differentiative capacities. Cartilaginous particles have been successfully created from human (h)ESCs and hiPSCs in laboratories including ours [16]. In order to create cartilage, hESCs and hiPSCs are initially differentiated toward chondrocytes, followed by transfer to a 3D culture, such as suspension culture or pellet culture, to make chondrocytes that produce and accumulate ECM [17]. hiPSC-derived cartilaginous tissue particles (hiPS-Cart) have been reported to form repair tissue after their implantation into AC defects in animal models [18], suggesting that they can be used for AC regeneration. Together with the fact that NP-ECM and AC-ECM share type II collagen (COL2), type XI collagen (COL11), and aggrecan (ACAN), the findings that hiPS-Cart also shares these ECM proteins [17] raises the hypothesis that hiPS-Cart can be used for NP regeneration.

NP cells are inhomogeneous and morphologically classified into at least two types: notochordal NP cells and chondrocyte-like NP cells. The former contains cells with vacuoles and assembles into masses of cell aggregates connected by intercellular junctions, whereas the latter is round in shape, dispersed, and surrounded by ECM [19,20]. Although microarray and bulk RNA sequencing (RNA-seq) analyses of NP and AC [21] and extensive proteomic analysis of NP [22] have determined the expression profile of NP as a whole, distinct profiles of notochordal NP cells and chondrocyte-like NP cells have not been clarified.

In the present study, we performed a single cell (sc)RNA-seq transcriptome analysis of NP and AC of cynomolgus monkey and compared the results with a scRNA-seq analysis of hiPS-Cart. Cell clustering analysis indicated that some NP cells and AC cells have similar transcriptomic profiles, suggesting that these cells in NP are chondrocyte-like NP cells. Marker gene expressions suggested that the remaining NP cells corresponded to notochordal NP cells. Notably, cells in hiPS-Cart had a transcriptomic profile similar to chondrocyte-like NP cells. To analyze the potential NP-function of hiPS-Cart, we employed a model in which NP was removed from the IVD of coccygeal vertebra in nude rats to cause substantial degeneration of the IVD and vertebral bone. hiPS-Cart implanted into the nuclectomized survived and prevented IVD and vertebral bone degeneration, indicating that hiPS-Cart can replace NP spatially and functionally. Mechanical tests indicated that the implantation of hiPS-Cart reverted the impaired mechanical properties of nuclectomized IVD toward those in sham-operated rats. Finally, we recovered the hiPS-Cart implants from rat IVD six weeks after the implantation and subjected them to scRNA-seq analysis. Post-implanted hiPS-Cart corresponded to chondrocyte-like NP cells but not to notochordal NP cells, suggesting that chondrocyte-like NP cells are sufficient for restoring the function of NP in our experimental animal model. These results collectively suggest that hiPS-Cart is a new tissue-engineered construct that can be used as an implant in regenerative therapy for the loss of NP to prevent IVD degeneration.

2. Materials and methods

2.1. Ethics statement

All methods were carried out in accordance with relevant guidelines and regulations. Experiments using recombinant DNA were approved by the Recombinant DNA Experiments Safety Committee of Kyoto University. Research involving human subjects was approved by the Ethics Committee of Kyoto University. Written informed consent was obtained from each donor. All animal experiments were approved by the institutional animal committee of Kyoto University.

2.2. Generation of hiPSC-derived cartilaginous tissue

The hiPSC line QHJI was generated from a healthy individual and was a kind gift from K. Okita, M. Nakagawa, and S. Yamanaka (Center for iPS Cell Research and Application (CiRA), Kyoto University, Kyoto, Japan). QHJI was generated by reprogramming human peripheral mononuclear cells by electroporating into them episomal plasmid vectors (pCXLE-hOCT3/4-shp53-F, hSK, hUL, EBNA) [23]. All cells were negative for genome integration.

hiPSCs were cultured in bioreactors and chondrogenically differentiated to produce hiPS-Cart following a previously described method using a bioreactor [24]. hiPS-Cart were generated by chondrogenic differentiation for 14 weeks and maintained in chondrogenic medium (DMEM (Sigma-Aldrich, USA) with 1% FBS (Thermo Fisher Scientific, USA), 1% ITS-X (Thermo Fisher Scientific, USA), 50 μg/mL ascorbic acid (nacalai tesque, Japan), 1 mM sodium pyruvate (Thermo Fisher Scientific, USA), 1% nonessential amino acids (Thermo Fisher Scientific, USA), 1% penicillin streptomycin (Sigma-Aldrich, USA), 10 ng/mL TGF-β1 (PeproTech, USA), 10 ng/mL GDF5 (ProSpec-Tany TechnoGene, Israel), and 10 ng/mL BMP2 (PeproTech, USA).

2.3. Single cell preparation for scRNA-seq analysis

A male 3-year-old cynomolgus monkey was sacrificed and dissected. Two NP samples (NP1 and NP2) from the lumber IVD (L4/5 and L5/6, respectively) and two AC samples (AC1 and AC2) from both knee joints were collected. In addition, to confirm reproducibility of the analysis, another male 3-year-old cynomolgus monkey was sacrificed, and a NP sample (NP4) from the lumber IVD (L4/5) was collected. Three rats implanted with hiPS-Cart were also sacrificed, and post-implant hiPS-Cart were harvested 6 weeks after the surgery. AC, pre-implant hiPS-Cart, and post-implant hiPS-Cart were minced into 1–2 mm pieces. Then the pieces and NP were digested with Liberase solution (for NP, AC, and

post-implant hiPS-Cart: RPMI-1640 (Nacalai Tesque) supplemented with 0.2% FBS, 10 mM HEPES pH7.2–7.4, 0.2–0.4 mg/mL Liberase TM (Roche), and 2 kU/mL DNase I (Merck); for pre-implant hiPS-Cart: DMEM with 1% FBS, 1% ITS-X, 50 μg/mL ascorbic acid, 1 mM sodium pyruvate, 1% nonessential amino acids, 1% penicillin streptomycin, 10 ng/mL TGF-β1, 10 ng/mL GDF5, and 10 ng/mL BMP2, 0.2 mg/mL Liberase TM (Roche), and 2 kU/mL DNase I (Merck) at 37 °C, 5% CO_2 for 120–210 min with sustained shaking. The cells were agitated 10 times with 1000 μL blue tip and then passed through a 70 μm cell strainer *(BD Biosciences)*, centrifuged at 4 °C for 300×*g* for 5 min, and their supernatant was discarded. The cells were resuspended in RPMI-1640 supplemented with 0.2% FBS and 10 mM HEPES.

For cell hashing, we biotinylated cell surface proteins with EZ-Link Sulfo–NHS–Biotin (Thermo Scientific), followed by staining with 0.6 μg/mL of Totalseq (A0951-A0955, and A0436 (BioLegend)) (Details of the method will be described elsewhere.) Cells that were alive and stained with A0951-A0955 were selected by flow cytometry using a FACS Aria II flow cytometer (BD Biosciences) and suspended in Sample Buffer (BD Biosciences).

2.4. cDNA synthesis and exonuclease I treatment by BD Rhapsody system

Obtained single-cell suspensions were subjected to a BD Rhapsody system with the BD Rhapsody Targeted & Abseq Reagent Kit (BD Biosciences) following the manufacturer's instructions. After reverse transcription, Exonuclease I treatment of the resultant BD Rhapsody beads was performed at 37 °C for 60 min and 1200 rpm on a Thermomixer C with a Thermotop. The resultant beads were immediately chilled on ice. The supernatant was removed, and the beads were washed with 1 mL WTA wash buffer (10 mM Tris-HCl pH8.0, 50 mM NaCl, 1 mM EDTA, 0.02% Tween-20) and 200 μL BD Rhapsody lysis buffer (for inactivation of enzyme), once again with 1 mL WTA wash buffer alone, twice with 500 μL WTA wash buffer, then resuspended with 200 μL Beads resuspension buffer and stored at 4 °C. During the washing step, bead-containing DNA LoBind tubes were replaced twice.

2.5. TAS-seq library generation

TAS-Seq libraries were generated by Immunogeneteqs Inc. (Noda city, Chiba, Japan) according to a previous report [25]. Briefly, reverse-transcribed, exonuclease I-treated BD Rhapsody beads were subjected to a terminator-assisted TdT reaction, second-strand synthesis reaction, and a 1st/2nd round of whole-transcriptome amplification (WTA) or Totalseq library amplification reaction. The size distribution and concentration of the amplified cDNA libraries and hashtag libraries were analyzed using a MultiNA system (Shimazu). Illumina libraries were constructed from 100 ng of amplified cDNA libraries using a NEBNext Ultra II FS library prep kit for Illumina (New England Biolabs). Illumina adapters and unique-dual barcodes were added to the hashtag libraries by PCR. The size distribution and concentration of the amplified Illumina libraries were analyzed using the MultiNA system and KAPA library quantification kit (KAPA Biosystems). Sequencing was performed using an Illumina Novaseq 6000 sequencer (Illumina, San Diego, CA, USA) and a Novaseq 6000 S4 reagent kit v1.0 or v1.5 according to the manufacturer's instructions (read 1 (cell barcode): 67 base-pair and read 2 (cDNA): 140 (v1.0)/155 (1.5) base-pair with 8 base-pair × 2 unique-dual indexes). The pooled library concentration was adjusted to 1.75 nM (v1.0) or 2.0 nM (v1.5), and 12% PhiX control library v3 (Illumina) was spiked into the library.

2.6. Fastq data preprocessing and generation of the single-cell gene-expression matrix

To obtain gene-expression count matrix and Totalseq expression matrix of each single cell, fastq files of the TAS-Seq data were processed by Immunogeneteqs Inc. as described previously [25]. For assignment of

cDNA reads to each transcript, bowtie2-indexes built from reference RNA sequences (cDNA and ncRNA fasta files of the Ensembl database (Macaca_fascicularis_6.0 for macaca fascicularis data, and GRCh38 release-101 for human data) [26]) were used. Associated Totalseq streptavidin/anti-biotin reads were mapped to known barcode sequences (provided by BioLegend) using bowtie2-2.4.2 with the following parameters: p 2 -D 20 –R 3 –N 0 -L 8 -i S,1,0.75 -norc -seed 656565 -reorder -trim-to 3:39 -score-min L,-9,0 -mp 3,3 -np 3 -rdg 3,3. The inflection point of the knee-plot (total read count versus the rank of the read count) was detected using the DropletUtils package [27] in R 3.6.3 (https://cran.r-project.org/) from the resulting single-cell gene-expression matrix files. Cells for which the total read count was over the inflection point were considered as valid cells. Demultiplexing of single cells by the expression of Totalseq streptavidin/anti-biotin was performed as described previously [25].

2.7. Background subtraction of TAS-Seq expression matrix by distribution-based error correction

To reduce the background read counts of each gene that were possibly derived from RNA diffusion during the cell lysis step within the BD Rhapsody cartridge and reverse transcription, a distribution-based error correction that is included in the BD Rhapsody targeted scRNA-seq workflow was performed by Immunogeneteqs Inc. as previously reported [25]. Briefly, the genes for which the $log_2(x+1)$-transformed maximum expression was over 8 were selected, a biexponential transformation was applied to each gene count using the FlowTrans package [28] in R 3.6.3. Next, Gaussian mixture components were detected using the mclust package [29] in R 3.6.3, the average expression of each component was calculated, and the genes for which the maximum average expression of each component was over 5.5 were selected. Then, if the difference of the average expression of each component against its maximum expression was greater than 5, the expression level of the components was considered to be background gene expression, and the converted expression of the components was set to 0.

2.8. Single-cell clustering and annotation

We clustered single cells of each dataset using Seurat v4.0 [30] in R 4.1.0. The Seurat object for each dataset was created using the CreateSeuratObject function (min.cells = 5, min.genes = 500). Cells in which the mitochondrial gene percentage was over the threshold indicated in Fig. S1A were filtered out by the subset function in Seurat v4.0. The expression data was normalized by the NormalizeData function (scale.factor = 1,000,000 according to the analytical parameter used by Tabula Muris [31]). Cells were categorized into S, G1, or G2/M phase by scoring cell cycle-associated gene expressions using the CellCycleScoring function. Highly variable genes in each dataset were identified using the FindVariableFeatures function with the following parameters: selection.method = "vst", nfeatures = 5000, mean.cutoff = c(0.1, Inf), and dispersion.cutoff = c(0.5, Inf). The expression data was scaled with the ScaleData function. Read counts of each cell within each dataset were regressed as a confounding factor in the ScaleData function. Principal component analysis (PCA) was performed using the RunPCA function, and the top 42 PCs were selected to perform dimensional reduction using uniform manifold approximation and projection (UMAP). We determined a cluster resolution of values as indicated in the Results section. Differentially expressed genes (DEGs) of each cluster were determined by the FindMarkers function with a 0.05 p_val_adj threshold between two groups (i.e., cell clusters).

DEGs were further analyzed by ingenuity pathway analysis (IPA) (QIAGEN) to determine upstream genes and pathway identification.

2.9. SingleR

Cells in hiPS-Cart before implantation and after implantation were

annotated using SingleR v1.7.0 [32]. We used NP and AC datasets as references.

2.10. RNA velocity analysis

For the RNA velocity analysis, TAS-Seq data cDNA reads were mapped to the reference genome (Macaca_fascicularis_6.0 for macaca fascicularis data, and GRCh38 release-101 for human data) using HISAT2-2.2.1 [33] and the following parameters: q -p 6 –rna-strandness F –very-sensitive –seed 656565 –reorder –omit-sec-seq –mm. For the HISAT2 index build, a corresponding ensembl gtf file was filtered to retain protein-coding RNA, long non-coding RNA, and T cell chain/immunoglobulin chain annotations according to the 10X Genomics's method (support.10xgenomics.com/single-cell-gene-expression/soft ware/pipelines/latest/advanced/references" title="https://support. 10xgenomics.com/single-cell-gene-expression/software/pipelines/ latest/advanced/references">https://support.10xgenomics.com/sin gle-cell-gene-expression/software/pipelines/latest/advanced/refer ences#mkgtf). Then, the cell barcode information of each read was added to the HISAT2-mapped BAM files, and associated gene annotations were assigned using featureCounts v2.0.2 [34] and the following parameters: T 2 -Q 0 -s 1 -t gene -g gene_name –primary -M –O –largestOverlap –fraction –R BAM. In the featureCounts analysis, a "gene" annotation was used to capture unspliced RNA information for the RNA velocity analysis, and primary annotations were kept. The resulting BAM file was split using valid cell barcodes and nim 1.0.6 and hts-nim v0.2.23, the split files were processed into loom files using velocyto run (vesion 0.17.17) with the -c and -U options, and the loom files were concatenated using the loompy.combine function (version 3.0.6) [35]. Then, we performed RNA velocity analysis using scVelo [36]. We read the loom files to an AnnData object. After estimating the RNA velocity, we inferred the trajectory using PAGA [37], which was extended by the velocity-inferred directionality. We also performed dynamical modeling velocity analysis.

2.11. Implantation of human iPS-Cart in a rat tail nuclectomy model

Nude rats (8-week-old males) were subjected to the operation and divided into four groups (Fig. 2B). Rats were anesthetized by injecting three types of mixed anesthetic agents (15 μg of medetomidine hydrochloride, 80 μg of midazolam, and 100 μg of butorphanol tartrate) into the gluteal muscle. The surgical procedures are shown in Fig. S3A and Movies 1–3. The dorsal skin at the level of the 6th coccygeal vertebra (Co6) and Co7 was incised longitudinally, and the dorsal side of the intervertebral disk between Co6 and Co7 was exposed. NP was removed totally with a micro curette of size 1 mm through the portal created by a longitudinal incision in AF. We trimmed the hiPS-Cart into a cylindrical shape with a diameter of 1.5 mm and height of 2 mm using a biopsy punch and inserted it into the nuclectomized space through the portal through which we had removed NP from the IVD. After implantation, AF and the skin were closed using 5-0 nylon sutures. To limit the tail movement and protect the wound, the operated site was immobilized with 5-cm-wide tape and then wrapped with ratproof tape to prevent biting for 1 week postoperatively (Fig. S3B). At 6 weeks or 6 months after surgery, the rats were euthanized by carbon dioxide inhalation, and samples, including the operated IVD and adjacent rostral and caudal vertebrae were harvested.

Supplementary video related to this article can be found at https://doi.org/10.1016/j.biomaterials.2022.121491

A total of 98 nude rats were used. For sacrifice at 6 weeks after surgery, 24 rats were used for the radiography and micro-computed tomography (micro-CT) analysis and 20 rats for the histological analysis; another 6 rats with sham operation were used for the radiography, micro-CT and histological analyses; still another 3 rats with retained hiPS-Cart implantation were used for scRNA-seq analysis. For sacrifice at 6 months after surgery, 23 rats were used for the radiography, micro-

CT and histological analyses and another 22 rats for the radiography, micro-CT and mechanical test analyses. The number of rats in each group is indicated at the bottom of the graphs shown in the figures.

2.12. Magnetic resonance imaging

Rats underwent T2-weighted sagittal magnetic resonance imaging (ICON 1T, Bruker, USA) in the prone position after anesthesia 1 week after surgery using the following settings: TR = 4000 ms, TE = 78 ms, field of view = 30*15 mm, and section thickness = 1.0 mm. Visualization was performed using ImageJ software (National Institutes of Health, Bethesda, MD, USA). In rats that received hiPS-Cart implants, retainment or dislodgement of hiPS-Cart was judged based on the presence or absence of a high intensity area in IVD in the MRI images (Fig. 2C). Two independent individuals made the judgment in a blinded manner.

2.13. Radiograph assessment of the disk height and micro-computed tomography of the epiphyseal bone

Radiography and micro-CT of rats were sequentially taken using a microfocus X-ray CT system (inspeXio SMX-100CT, Shimadzu Corporation, Japan) before surgery and at 6 weeks or 6 months after surgery. After anesthesia, a radiograph area covering the operated IVD and adjacent rostral and caudal vertebrae was taken (80 μA, 60 kV, 2 averages, and 1 feed line). The disk height index (DHI) was measured using ImageJ software following a previous report [38]. The disk height and adjacent vertebral body heights were measured ventrally, centrally, and dorsally, and the DHI was calculated by dividing the sum of the disk heights by the average of the sum of the adjacent vertebral body heights and multiplying by 100. The DHI at 6 weeks and 6 months after surgery was divided by the DHI before surgery to calculate %DHI for each sample.

As for micro-CT, an area covering the operated IVD and adjacent rostral and caudal vertebrae was scanned (80 μA, 60 kV, 1200 views, 4*1 averages, and full scan angle). The epiphyseal bone volume (BV) adjacent to the operated IVD was measured at 6 weeks after surgery using TRI/3D-BON-FCS (RATOC System Engineering, Japan) (Fig. 3E). The %BV was calculated by dividing the BV at 6 weeks after surgery by the BV before surgery. At 6 months after surgery, the epiphysis was so severely destructed that we could not measure the BV. Therefore, we measured the area in which the bone had eroded from the end line of the epiphysis and called the area the "bone erosion area". We summed bone erosion areas of the caudal epiphysis of Co6 and rostral epiphysis of Co7 (Fig. S4E).

2.14. Histology and immunohistochemistry evaluation

Rats were euthanized at 6 weeks or 6 months after surgery. Specimens were harvested, fixed in 4% paraformaldehyde, decalcified with 10% EDTA for 4–5 weeks, dehydrated in graded ethanol, and embedded in paraffin wax. 3-μm coronal sections were prepared. Semi-serial sections were stained with hematoxylin and eosin (HE) or Safranin-O-fast green-iron hematoxylin (Safranin O). For immunostaining, paraffin-embedded sections were deparaffinized and incubated in 1 mM EDTA buffer (pH 8.0) at 80 °C for 15 min to retrieve the antigen. Then the sections were treated with 10 mg/mL hyaluronidase at 37 °C for 30 min. After peroxidase and protein blocking, the sections were incubated with primary antibody overnight at 4 °C. The following primary antibodies were used: rabbit anti-human vimentin (Abcam, 1:400), mouse anti-type II collagen (Thermo Scientific, 1:2000) and rabbit monoclonal anti-human aggrecan (Abcam, ab186414, 1:1000). The primary antibodies were detected with a CSA II Biotin-free Tyamide Signal Amplification System Kit (Agilent Technologies, USA) and DAB as a chromogen.

Histological grading was performed based on the presence or absence of the safranin O-positive area and the structure of bone and

cartilage in the adjacent vertebrae (Supplementary Table 2). The total score was calculated according to the degree of degeneration and ranged from 0 to 6, which denote normal and severe degeneration, respectively.

2.15. Biomechanical test

Biomechanical tests were performed as in a previous report using axial cyclic tension-compression tests to assess the dynamic viscoelastic properties of the IVDs [39]. Rats were euthanized by carbon dioxide inhalation at 6 months after the implantation of hiPS-Cart, followed by explanting samples, including the operated IVD and adjacent vertebrae, and removing as much surrounding tissue as possible. The vertebral bodies of the specimens were coated by bone cement (Ostron II, GC Corporation, Japan) and held and attached to a dynamic mechanical analyzer (ElectroForce 5500, TA Instruments, USA). Specimens were placed in a testing chamber filled with 37 °C saline. Compressive stress of 0.1 MPa was applied from the zero-load point as pre-stress, followed by relaxation for 30 min, and then sinusoidal compressive and tensile displacements with 0.1 mm amplitude were applied at frequencies of 0.05, 0.1, 0.5, 1.0 and 5.0 Hz. The storage modulus and loss modulus of the IVDs were measured respectively.

2.16. Statistical analysis

Prism ver. 8.0.2 (GraphPad Software, USA) and R 4.1.1 were used for the statistical analysis. All results are reported as the mean ± standard deviation. One-way analysis of variance (ANOVA) with post-hoc Tukey HSD test or Student's t-test were used to compare the %DHI, %BV, and bone erosion area. The Steel-Dwass test or Mann-Whitney *U* test was used for the histological score. Two-way ANOVA with a post-hoc Tukey HSD test was used for the mechanical test data. P values < 0.05 were considered statistically significant.

3. Results

3.1. Single cell transcriptome analysis identified chondrocyte-like NP cells and notochordal NP cells, and hiPS-Cart cells corresponded to chondrocyte-like NP cells

We differentiated hiPSCs toward chondrocytes in chondrogenic medium. Then we transferred the hiPSC-derived chondrocytes to suspension culture to make them produce and accumulate ECM, resulting in the formation of cartilaginous particles (hiPS-Cart) with diameters of 2–3 mm (Fig. 1A). Histology analysis indicated that hiPS-Cart consisted of cells embedded in abundant ECM that were positively stained with safranin O (Fig. 1B) and immunostained with anti-COL2 and anti-ACAN antibodies (Fig. 1C).

To investigate how similar hiPS-Cart is to native cartilage or NP, we performed scRNA-seq analysis. As for the target tissues, we analyzed AC and NP from cynomolgus monkey, because we could acquire intact tissue from primates. The samples analyzed in the present study are described in Fig. S1A. A Ridgeplot (Seurat) analysis of the normalized expression confirmed that no cells in hiPS-Cart expressed pluripotent markers (*POU5F1* and *LIN28A*) (Fig. 1D; Fig. S1B). Most hiPS-Cart cells expressed chondrogenic markers, including *COL2A1*, *COL11A2* and *ACAN*, at levels comparable to or higher than AC cells and NP cells. *PRG4* (also known as *SZP* or *LUBRICIN*), which is specifically expressed in the superficial zone of AC [40], was expressed at a very high level by some AC cells (Fig. 1D, arrow). Of note, markers for notochord-like cells, such as *KRT19* and *TBXT* (also known as *T*), were expressed highly by only some NP cells (Fig. 1D, arrowheads), suggesting heterogeneity in the NP cell population. hiPS-Cart cells expressed neither *KRT19* nor *TBXT* highly.

Next, the scRNA-seq data of NP and AC were subjected to unsupervised clustering and visualized using uniform manifold approximation and projection (UMAP) plots (Fig. 1E). NP and AC cells were separated clearly into three clusters (Fig. 1E). Cluster #0 consisted of almost only AC cells, #1 consisted of AC cells and NP cells, and #2 consisted of only NP cells (Fig. 1E and F; Fig. S2A). The FeaturePlot function in Seurat [30] revealed that the cells in cluster #0 expressed *PRG4* highly (Fig. 1G), suggesting they are superficial zone cells in AC. Cluster #2 cells expressed *COL2A1* less and *ACAN* more than cluster #1 cells (Fig. 1G) and exclusively expressed KRT19 (Fig. S2B), suggesting that they are notochordal NP cells. The FindMarkers function in Seurat [30] revealed multiple genes (Fig. S2C), including genes previously reported as notochordal NP cell-specific (*KRT19*, *TBXT*, CA3 and *SHH*) [20,21,41, 42] and previously unreported (*APOE*, *C3orf49*, and others), that were exclusively expressed in cluster #2 (Fig. S2B). Cluster #1 cells highly expressed chondrocyte markers (*COL2A1* and *COL11A2*) (Fig. 1E,G), suggesting that they are chondrocytes in AC and chondrocyte-like NP cells.

To determine to which of AC or NP hiPS-Cart cells correspond, we annotated hiPS-Cart cells against the three clusters described above as a reference using SingleR [32]. All cells in hiPS-Cart were exclusively annotated to cluster #1 (chondrocytes in AC and chondrocyte-like NP cells; Fig. 2A). These results suggest that hiPS-Cart have a transcriptomic profile that is shared by chondrocytes in AC and chondrocyte-like NP cells. Although multiple studies have shown that the implantation of hiPS-Cart successfully regenerates AC defects in animal models [16,18], our findings further suggest that the implantation of hiPS-Cart can regenerate the loss of NP. To test this hypothesis, we performed animal experiments using nude rats.

3.2. Animal model experiments in which hiPS-Cart was implanted into nulectomized space of nude rat IVD

We divided nude rats into four groups (Fig. 2B). We made a skin incision over the IVD of coccygeal vertebra of nude rats (Fig. 2B). We closed the incision without intervention in some rats (Sham group) and removed NP from the IVD in others (Fig. 2B; Fig. S3Ab). Then we implanted nothing (Nuc group) or hiPS-Cart (Fig. S3Ae,f) into the nuclectomized space (Fig. 2B). Rats moved their tails vigorously immediately after recovery from the anesthesia for surgery; this motion appeared to cause dislodgement of the hiPS-Cart implants at the early period after surgery. To control the occurrence of this dislodgement, we restricted the motion of the implanted sites by wrapping the rats with tape (Fig. S3B). We then subjected the rats that received hiPS-Cart implantation to MRI imaging one week after the implantation (Fig. 2B and C). MRI detected NP as a high intensity area in the IVD of the sham group, but no such high intensity area was observed in the Nuc group, suggesting that entire NP was removed. Among the rats which received the hiPS-Cart implantation, we allocated them to either the hiPS-Cart Dislodged group or hiPS-Cart Retained group based on the absence or presence of a high intensity area in the MRI images (Fig. 2B and C). All rats were sacrificed at 6 weeks or 6 months after surgery, and samples were collected and subjected for analysis.

3.3. Radiographic evaluation indicated that hiPS-Cart prevented destruction of endplate structure

At six weeks after the implantation surgery, lateral radiographs of the samples revealed irregularities in both the rostral and caudal endplates in all samples in the Nuc group (Fig. 3A). The hiPS-Cart Dislodged group also showed evidence of endplate irregularity. On the other hand, the hiPS-Cart Retained group showed a smooth surface with no irregularity in the endplates. The reduced width of the space of vertebral bone (disk height) in the radiographic image represents the degree of IVD degeneration. The hiPS-Cart Retained group showed a significantly higher % disk height index (%DHI) than the Nuc group (Fig. 3B). Furthermore, when data from the hiPS-Cart Dislodged group and hiPS-Cart Retained group were combined, the %DHI was still significantly higher than that of the Nuc group (Fig. 3C). Similar observations were
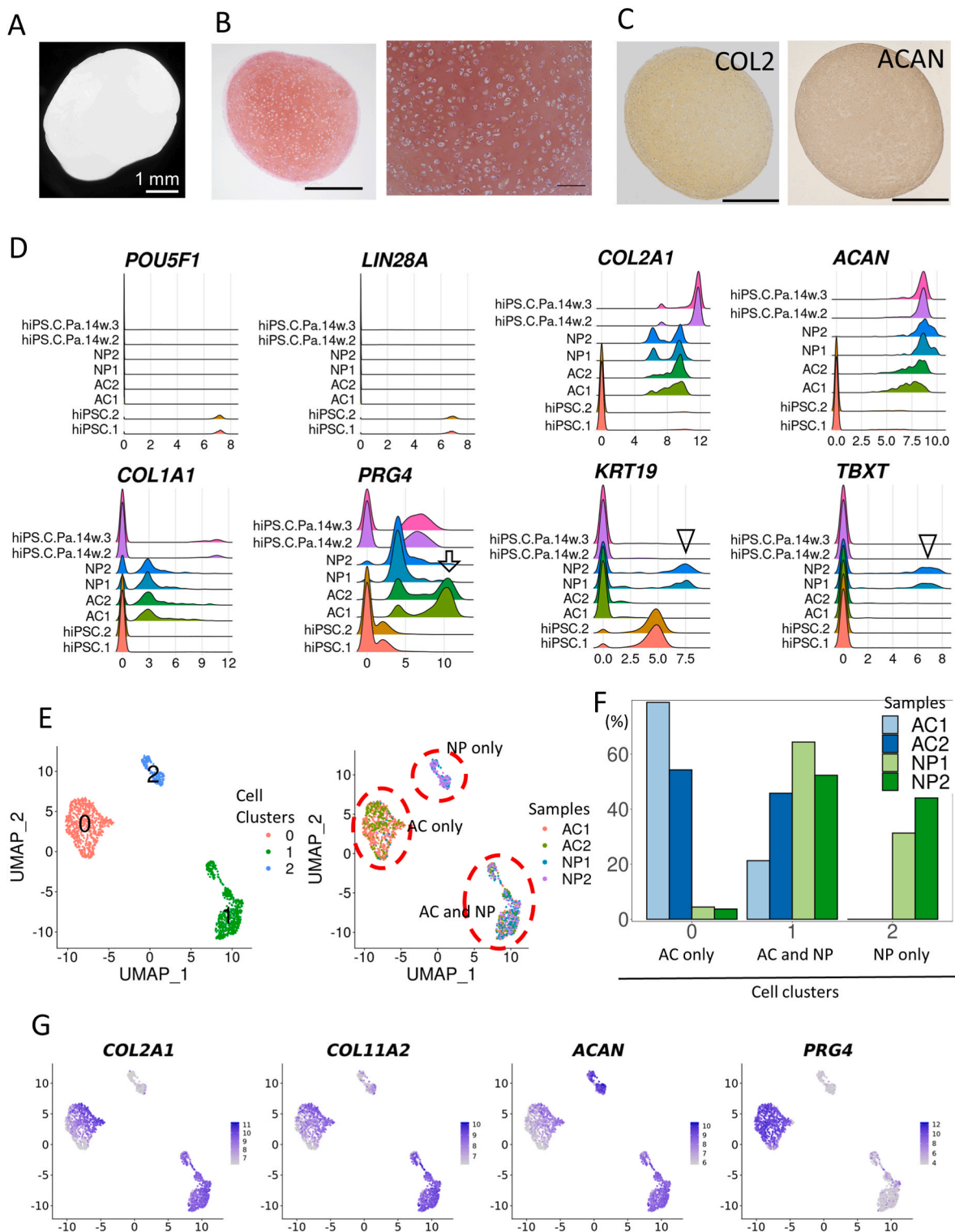
Fig. 1. Characterization of hiPSC-derived cartilaginous tissue (hiPS-Cart), NP, and AC by scRNA-seq. A) Gross appearance of hiPS-Cart. B) Histology of hiPS-Cart. Safranin O-fast green-iron hematoxylin staining (safranin O). Scale bars: *left*, 500 μm; *right*, 100 μm. C) Immunohistochemistry of hiPS-Cart. Antibodies that recognize type II collagen (COL2) and Aggrecan (ACAN) were used. Scale bars: 500 μm. D-G) scRNA-seq analysis of hiPSCs, hiPS-Cart, monkey AC, and monkey NP. D) Ridgeplot (Seurat) showing the distribution of single cell gene expressions in each sample. The X-axis of each panel represents the expression level of the indicated gene. The Y-axis of each panel represents the number of cells. E) AC and NP cells were used to generate UMAP plots with the parameter resolution = 0.05. F) The percentage of each cell type in each sample is plotted. G) Marker gene expression levels are indicated in each cell projected on the UMAP plot using the FeaturePlot function. . (For interpretation of the references to colour in this figure legend, the reader is referred to the Web version of this article.)
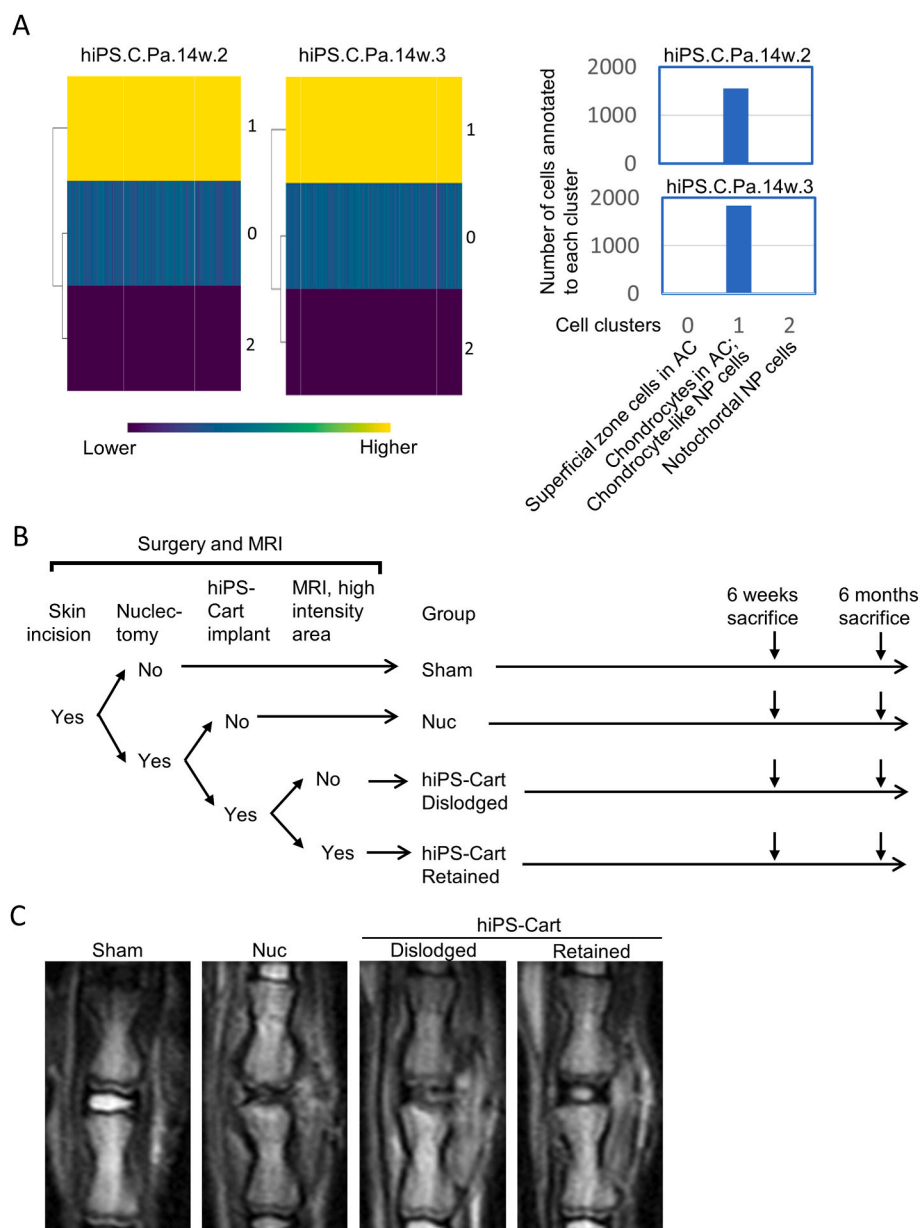
Fig. 2. Annotation of hiPS-Cart cells by scRNA-seq data and design of implantation experiments in rat. A) We annotated hiPSC-Cart cells against the three clusters discovered in monkey AC and NP as a reference using SingleR. *Left*, PlotScoreHeatmap function. The scores for all cells across all reference clusters are displayed. *Right*, The number of cells that were annotated to each type were calculated using SingleR functions and plotted. B) The four groups of rats in which hiPS-Cart was implanted into the nuclectomized space. C) Representative MRI images of the treated sites in each of the four groups.

made at six months after surgery (Figs. S4A–C).

3.4. Micro-CT evaluation confirmed that hiPS-Cart implantation protected IVD from degeneration

At six weeks after surgery, micro-CT images revealed severe disruption of the endplate bone structure in the Nuc group (Fig. 3D). The same was true for the hiPS-Cart Dislodged group. In contrast, the hiPS-Cart Retained group indicated preserved endplates. The mean % of bone volume (%BV) of the endplate bone in the hiPS-Cart Retained group was significantly higher than that of the Nuc group and not significantly different from that of the Sham group (Fig. 3E and F). When the data of the hiPS-Cart Dislodged and hiPS-Cart Retained groups were combined, the %BV of their endplate bone was still significantly higher than that of the Nuc group (Fig. 3G). As with the radiography analysis, similar observations were made at six months after surgery (Figs. S4D–G): the mean bone erosion area of the hiPS-Cart Retained group was significantly lower than that of the Nuc group and not significantly different from that of the Sham group (Figs. S4E and F); and when the data of the

hiPS-Cart Dislodged and hiPS-Cart Retained groups were combined, their bone erosion area was still significantly lower than that of the Nuc group (Fig. S4G).

3.5. Histology assessment revealed that implanted hiPS-Cart survived, occupied NP space, and prevented IVD destruction

At six weeks after surgery, histology analysis revealed that NP was absent, and the layered structure of AF was disrupted in the Nuc group and in the hiPS-Cart Dislodged group (Fig. 4A; Fig. S5). In addition, bone was destroyed, and cartilage showed irregularity or discontinuity. On the other hand, the hiPS-Cart Retained group showed cartilaginous tissue in the NP space and nearly normal structures of AF, bone, and cartilage. The inner layer of AF was thickened to fill the space created by the smaller width of the cartilaginous tissue compared with the width of NP and was stained strongly with Safranin O compared to AF in the Sham group (Fig. 4A; Fig. S5). Immunohistochemical analysis revealed that cartilaginous tissue in the NP space and thickened inner layer of AF in the hiPS-Cart Retained group expressed COL2 moderately and ACAN
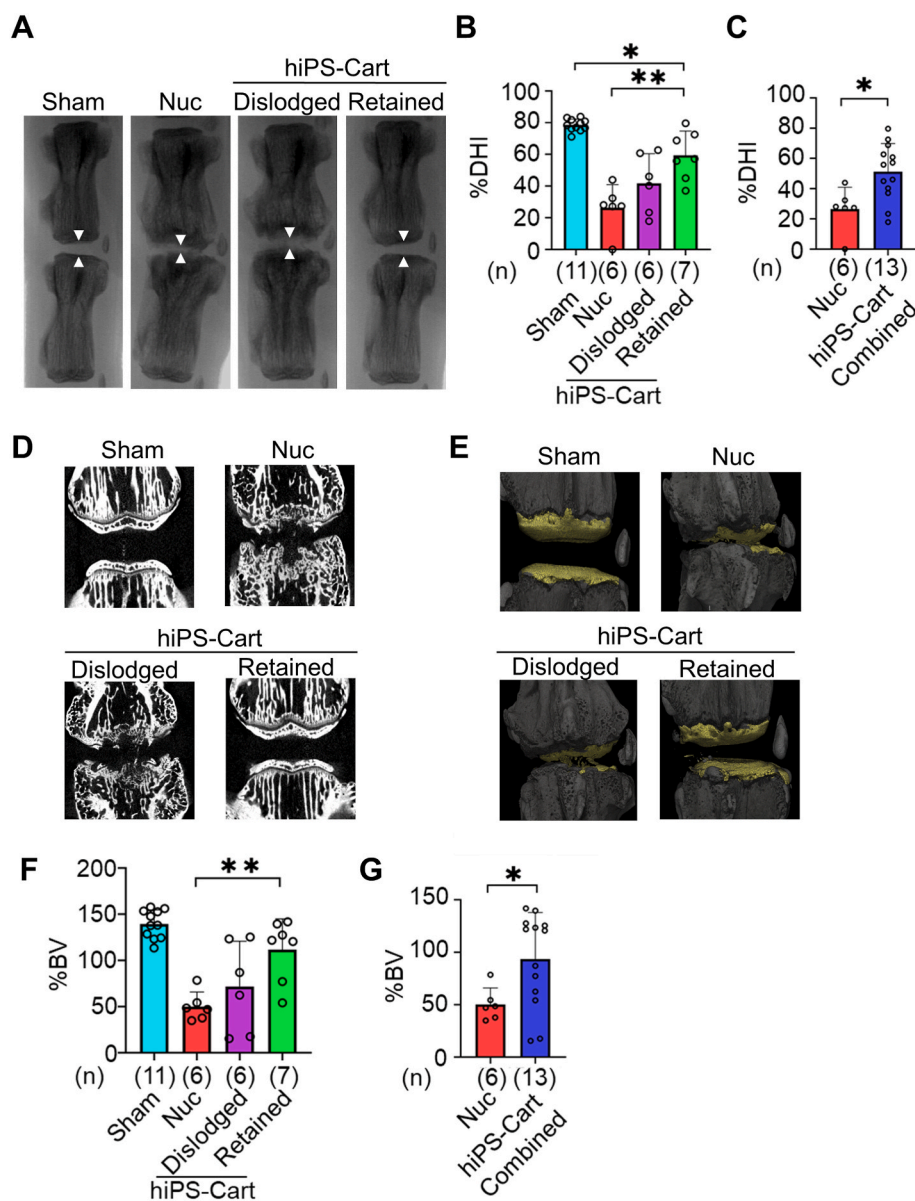
Fig. 3. Radiography and micro-CT evaluation of rat IVD six weeks after surgery. A) Representative lateral radiographs of treated sites in each of the four groups. Disk heights are indicated by the distances between the arrowheads. B) % disk height index (%DHI) for each group. C) The %DHI data for the hiPS-Cart Dislodged group and hiPS-Cart Retained group were combined into one group (hiPS-Cart Combined group) and plotted. D, E) Representative micro-CT images of treated sites in each of the four groups. Coronal images (D). 3D images were reconstructed (E). Epiphyseal bone is indicated in yellow. F) Epiphyseal bone volume (BV) was measured before and 6 weeks after surgery. % bone volume (%BV), which is the BV at 6 weeks after surgery divided by the BV before surgery, was calculated for each group. G) The BV data for the hiPS-Cart Dislodged group and hiPS-Cart Retained group were combined into one group (hiPS-Cart Combined group) and plotted. Each circle indicates one rat. *(n)*, numbers of rats for each group. Error bars denote means ± s.d. *P < 0.05, **P < 0.01 by one-way ANOVA with post-hoc Tukey HSD test (F) and Student's t-test (G). . (For interpretation of the references to colour in this figure legend, the reader is referred to the Web version of this article.)

strongly (Fig. 4A; Fig. S5) in the ECM. We used an anti-ACAN antibody that recognizes only human ACAN. hiPS-Cart appeared to produce ACAN that was secreted into and constituted ECM of the inner layer of AF (Fig. 4A). Positive immunoreactivity against an antibody that recognizes only human vimentin but not rat vimentin confirmed that the cartilaginous tissue in the NP space in the hiPS-Cart Retained group is human and therefore hiPS-Cart (Fig. 4A and B). There were some cartilaginous fragments, which appeared as either fragments of destructed growth plate cartilage or the inner layer of AF that underwent cartilaginous change under pathological conditions in the hiPS-Cart Dislodged group (Fig. 4A, black boxes). These cartilaginous fragments were human vimentin-negative (Fig. S6) and thus not remnants of hiPS-Cart. The histological score for the IVD structure of the hiPS-Cart Retained group was significantly lower than that of the Nuc group (Fig. 4C). When the data of the hiPS-Cart Dislodged and hiPS-Cart Retained groups were combined, their histological score for the IVD structure was still significantly lower than that of the Nuc group (Fig. 4D).

At six months after surgery, the Nuc group and the hiPS-Cart Dislodged group showed an absence of NP, disruption of layered AF, and

destruction of bone and cartilage (Fig. S7A). In contrast, the hiPS-Cart Retained group showed Safranin O-positive cartilaginous tissue in the NP space, and the surrounding tissue, such as layered AF, bone, and cartilage, was preserved (Fig. S7A). In addition, immunohistochemistry revealed that the cartilaginous tissue expressed COL2 in the ECM and human vimentin-positive cells (Figs. S7A and B), suggesting survival of the hiPS-Cart. The histological score for the IVD structure of the hiPS-Cart Retained group was significantly lower than that of the Nuc group (Fig. S7C). When the data of the hiPS-Cart Dislodged and hiPS-Cart Retained groups were combined, their histological score for the IVD structure was still significantly lower than that of the Nuc group (Fig. S7D). Observations of the hiPS-Cart Retained group indicated that hiPS-Cart and surrounding AF were avascular at both 6 weeks and 6 months after the implantation.

3.6. Biomechanical tests indicated that hiPS-Cart retained biomechanical properties of IVD

At six months after the implantation, a biomechanical test (Fig. 5A) revealed that the mean storage modulus of the hiPS-Cart Retained group
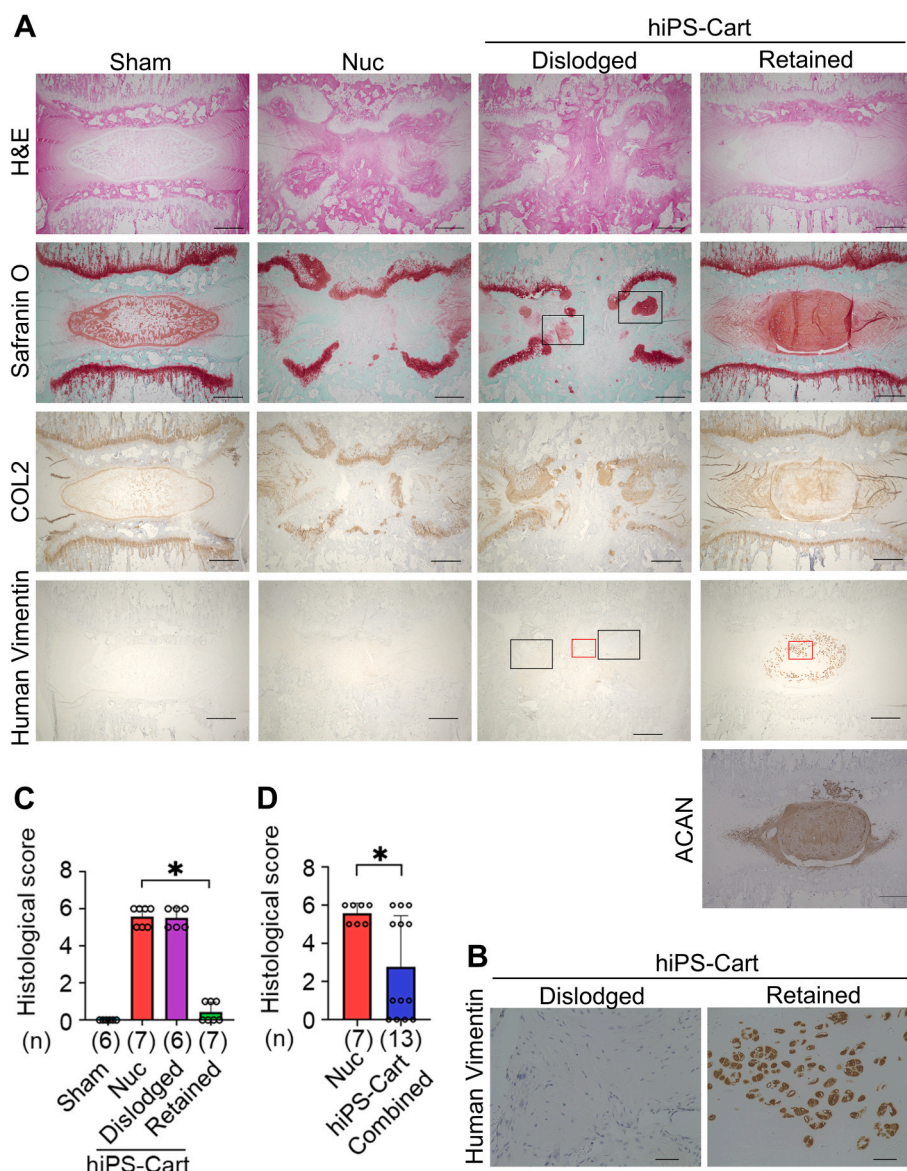
Fig. 4. Histological evaluation of rat IVD six weeks after surgery. A) Semi-serial histological sections of IVD from each group were stained with hematoxylin-eosin (top row) and safranin O-fast green-iron hematoxylin (second row) and immunostained with anti-COL2 antibody (third row), anti-human vimentin antibody (fourth row) and anti-ACAN antibody (bottom row). Anti-ACAN antibody recognizes only human ACAN and not rat ACAN. Black boxed regions are shown in Fig. S6. Red boxed regions are shown in (B). Scale bars, 500 μm. B) Magnified images of the red boxed regions in (A). Scale bars, 20 μm. C) Histological score for the structure of the IVD and vertebrae of each group. The histological grading scale is described in Supplementary Table 2. D) Histological scores of the hiPS-Cart Dislodged group and hiPS-Cart Retained group were combined into one group (hiPS-Cart Combined group) and plotted. Each circle indicates one rat. *(n)*, numbers of rats for each group. Error bars denote means ± s.d. *P < 0.05 by Steel-Dwass test (C) and Mann-Whitney *U* test (D). . (For interpretation of the references to colour in this figure legend, the reader is referred to the Web version of this article.)

was significantly lower than that of the Nuc group and not significantly different from that of the Sham group at every frequency tested (0.05–5.0 Hz) (Fig. 5B). Furthermore, the mean loss modulus of the hiPS-Cart Retained group was significantly different from that of the Sham group only at 0.5 Hz, whereas that of the Nuc group was significantly different from the Sham group at 0.05 Hz and 0.1 Hz (Fig. 5C). The frequency dependency of the loss modulus of the hiPS-Cart Retained group was more similar to that of the Sham group, with the highest value at 0.5 Hz, than to the Nuc group. These results collectively indicate that the biomechanical properties of hiPS-Cart Retained group were more similar to those of the Sham group than of the Nuc group.

3.7. Single cell transcriptome analysis of post-implant hiPS-Cart

We harvested hiPS-Cart implants six weeks after surgery, subjected them to scRNA-seq analysis, and compared the data with NP data from monkey and from hiPS-Cart before the implantation.

RidgePlot and DotPlot analyses indicated that most hiPS-Cart cells expressed chondrogenic markers, including *COL2A1*, *COL11A2* and *ACAN*, at levels comparable to or higher than AC cells and NP cells after the implantation (Fig. 6A; Fig. S8A). The expression levels of *PRG4* in

PRG4-positive cells in hiPS-Cart after implantation (Fig. 6A, disk. imp.3,4,6, arrow) decreased compared with the expression in hiPS-Cart before implantation (Fig. 6A, hiPS.C.Pa.14w.2,3, arrowhead), suggesting the absence of shear-stress signaling that activates *PRG4* expression in the environment of the NP space. No hiPS-Cart cells expressed the notochordal NP cell markers *KRT19* and *TBXT* after implantation.

To analyze how hiPS-Cart changed after implantation into the nuclectomized space, we annotated cells in hiPS-Cart before and after implantation against an NP dataset in which we separated cells into six clusters on a UMAP plot by employing the parameter resolution = 1.0 (Fig. 6B; Fig. S8B). Clusters #1 and #2 corresponded to notochordal NP cells, while clusters #0, #3 and #4 corresponded to chondrocyte-like NP cells, as indicated by the marker expression (Fig. 6C; Fig. S8C). Cluster #5 consisted of very few cells. SingleR [32] annotation against NP as a reference indicated that cells in hiPS-Cart before implantation corresponded mainly to clusters #0 and #3 (Fig. 7; Fig. S9). On the other hand, hiPS-Cart at 6 weeks after implantation mainly corresponded to clusters #3 and #4 (Fig. 7; Fig. S9). These results suggest that some hiPS-Cart cells changed their transcriptome profile after implantation in vivo. However, no hiPS-Cart cells became notochordal NP cells (clusters #1 and #2) after implantation. These results were reproduced using a
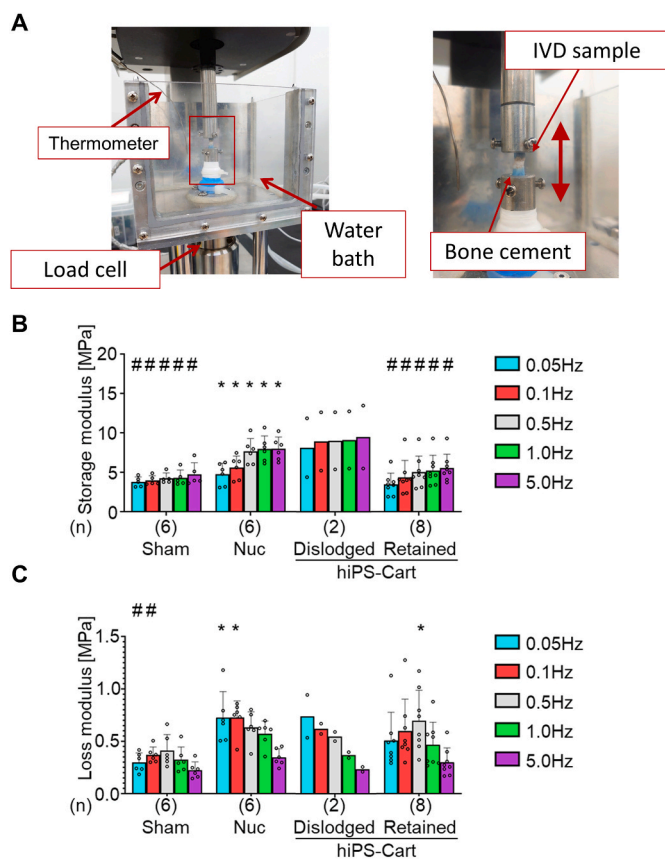
Fig. 5. Biomechanical testing of rat IVD six months after surgery. A) Left, image of the apparatus used for the mechanical test. Right, magnification of the left image. An IVD sample recovered from a nude rat was fixed in the apparatus with bone cement. A cyclic tension–compression axial load was applied. B, C) Results of the biomechanical test. The storage modulus (B) and loss modulus (C) were measured at various frequencies of cyclic tension–compression axial loads. The hiPS-Cart dislodged group consisted of two samples and was excluded from the statistical analysis. Each circle indicates one rat. *(n)*, numbers of rats for each group. Error bars denote means ± s.d. *P < 0.05 versus Sham group and #P < 0.05 versus Nuc group compared at each frequency by two-way ANOVA with post-hoc Tukey HSD test.

NP sample obtained from another monkey (Fig. S10).

To analyze how hiPS-Cart cells changed after their implantation into the nuclectomized space, we compared scRNA-seq data before and after implantation by integrating the datasets using Seurat canonical correlation analysis. Cells were separated into 6 clusters on a UMAP plot (Fig. 8A). Among them, clusters #2 and #3 were mainly composed of pre-implant hiPS-Cart, while clusters #0 and #1 were mainly composed of post-implant hiPS-Cart (Fig. 8B; Fig. S11A). These results suggest that the profiles of cells in clusters #2 and #3 changed to those in clusters #0 and #1 after implantation. To test this hypothesis, we performed an RNA velocity analysis of the post-implant hiPS-Cart scRNA-seq data using scVelo [36]. The trajectory inference using PAGA [37] that was extended by velocity-inferred directionality was consistent with the hypothesis and further revealed a branching event representing cell lineages (Fig. 8C). This finding suggests two trajectories from cluster #4 at the top of the hierarchy: one leads through cluster #2 to cluster #0, and the other leads through cluster #3 to cluster #1. To test these inferred trajectories, we ran the dynamical model of scVelo. The majority of directions of the velocity vectors projected onto UMAP embedding (Fig. 8D) were consistent with the directions of the trajectories (Fig. 8C, right). The FindMarkers function in Seurat and an ingenuity pathway analysis (IPA) (QIAGEN) revealed that the differentially expressed genes (DEGs) in cluster #4 (Fig. 8E; Fig. S11B)

were related to cell division (Fig. S11C). Consistently, cluster #4 cells had a high G2M.Score and S.Score (Fig. 8E) and therefore probably serve as proliferating progenitor cells for subsequent differentiation into different lineages.

Because the trajectory inference and RNA velocity analysis suggested that post-implant hiPS-Cart cells differentiate into two lineages that give rise to cluster #0 and cluster #1, respectively (Fig. 8C and D), we investigated the relevant events for this differentiation in post-implant hiPS-Cart. The FindMarkers function identified that cluster #0 highly expressed *DLK1* and *FRZB* and cluster #1 highly expressed *ASPN* and *TNC* (Fig. 8F). We then identified DEGs between clusters #0 and #1 and subjected them to IPA. Among the upstream regulators identified by the upstream analysis in IPA, BNIP3L, VEGF, and HIF1A (Figs. S12 and S13), respectively, had z-scores of 2.2, −5.1, and −2.5 (Supplementary Table 1), suggesting that BNIP3L was more activated and VEGF was more inhibited in cluster #0 than in cluster #1 and that HIF-1α was more activated in cluster #1 than in cluster #0.

4. Discussion

Understanding the biological roles of each cell type in NP and determining which cell types contribute to NP function are necessary for realizing NP regeneration against IVD degeneration [20]. NP cells are morphologically classified into two types: notochordal NP cells and chondrocyte-like NP cells (Fig. S14). Notochordal NP cells decrease with age, while chondrocyte-like NP cells increase and dominate by the age of 10 years old in human NP [20,42,43]. Although scRNA-seq is expected to help clarify each resident cell type of the NP compartment, recent reports that have analyzed NP cells using scRNA-seq have not identified notochord-like cells [44,45], probably because the samples were obtained from individuals older than 18 [44] or 37 [45] years old. In the present study, we identified notochordal NP cells and chondrocyte-like NP cells by employing a 3-year-old monkey, taking advantage of the intact young primate NP that can be sampled (Fig. S14). As for AC, cluster #0 cells and cluster #1 cells identified by the scRNA-seq analysis (Fig. 1E) appear to respectively correspond to superficial zone cells and middle/deep zone chondrocytes (Fig. S14). Chondrocyte-like NP cells and middle/deep zone chondrocytes in AC were positioned at identical locations (cluster #1 in Fig. 1E) in the UMAP plot and thus are transcriptomically similar.

Additionally, we found that hiPS-Cart, when implanted in the nuclectomized space, prevented IVD from nuclectomy-induced degeneration. In addition, mechanical tests proved that the mechanical properties of IVD units were preserved by implanting hiPS-Cart into the nuclectomized space. These results suggest that hiPS-Cart can replace NP functionally. However, the scRNA-seq analysis also revealed that cells in hiPS-Cart represent only part of the heterogenous NP cell population. hiPS-Cart neither before nor after implantation included the notochordal NP cell type and only corresponded to chondrocyte-like NP cells. Consistently, a histology analysis showed that hiPS-Cart morphologically resembles cartilage but not notochord. The cartilaginous morphology of hiPS-Cart was maintained at least 6 months after the implantation and preserved the surrounding IVD structure for this period. These results suggest that the cartilaginous element can perform the NP function that maintains the IVD structure.

NP cells reside in the avascular and hypoxic microenvironment of the IVD and thus are thought to metabolically rely on glycolysis for energy production through HIF-1α activation and to contain few functional mitochondria due to the induction of mitophagy [46]. Metabolic regulation in the hypoxic NP microenvironment is complex, as mice in which HIF-1α is inactivated in Foxa2-positive cells in NP do not show a decrease in mitophagic flux [46]. Post-implant hiPS-Cart resided in the avascular and hypoxic microenvironment, which appears responsible for alterations in the transcriptome profile after implantation. The trajectory inference and RNA velocity analysis indicated that post-implant hiPS-Cart give rise to two cell lineages. An IPA of DEGs between the two
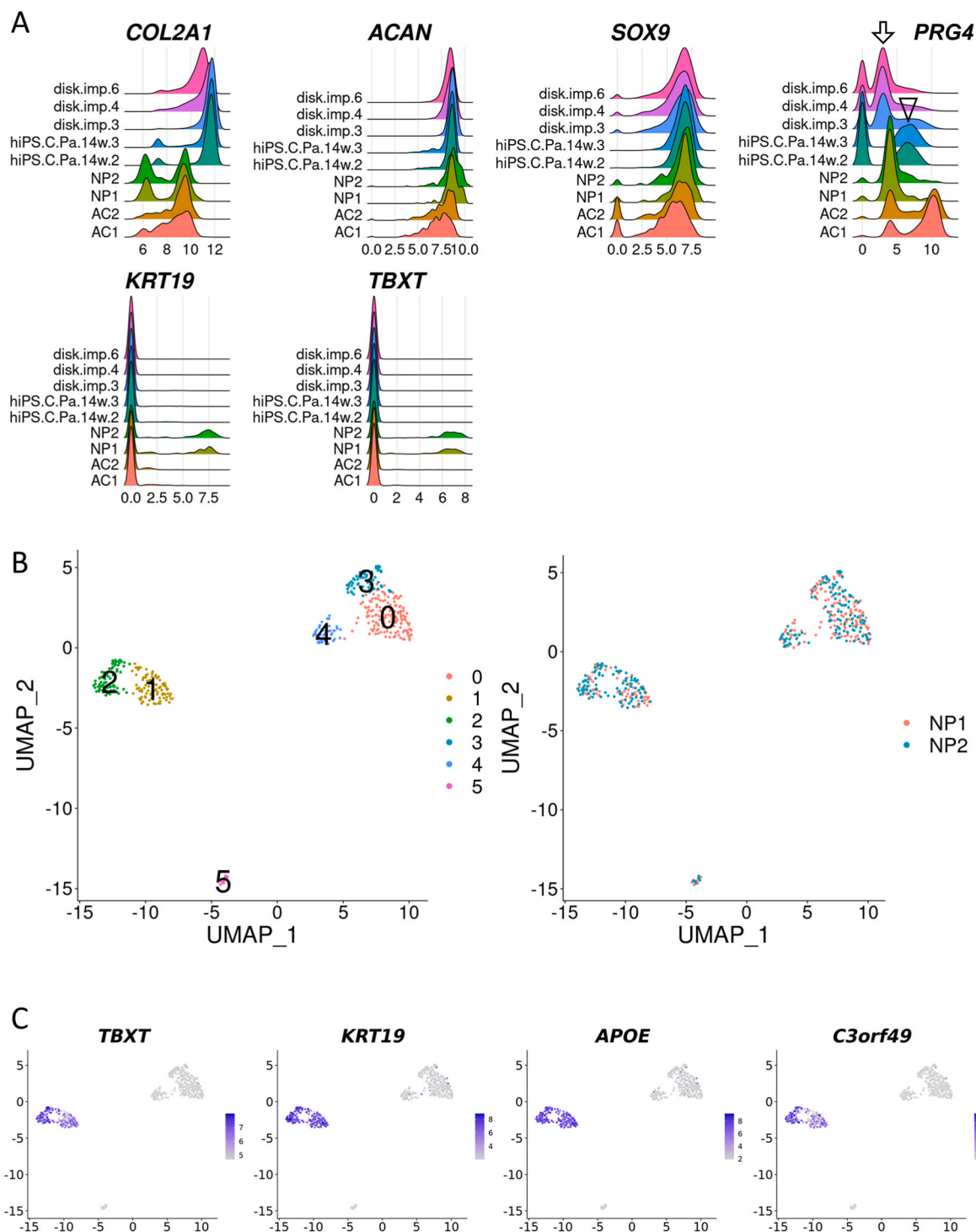
Fig. 6. Characterization of post-implant hiPS-Cart and UMAP plot of NP cells. A) Ridgeplot of marker expressions for each sample. B) NP cells were used to generate UMAP plots with the resolution parameter = 1. NP cells were separated into six clusters. C) The marker gene expression level is indicated for each cell projected on the UMAP plot using the FeaturePlot function.

lineages suggested distinct regulatory molecules for each. One cell lineage (cluster #0 in Fig. 8) showed activated BNIP3L signaling that mediates mitophagy [47] and inhibited VEGF signaling, whereas the other cell lineage (cluster #1 in Fig. 8) showed activated HIF-1α signaling. These findings suggest that post-implant hiPS-Cart cells adapted to the hypoxic microenvironment of NP distinctly in each lineage, functioning as NP to prevent IVD degradation.

Mouse lineage tracing studies have shown that notochordal NP cells and chondrocyte-like NP cells are derived from notochord cells [48,49].

Although it is unknown whether the loss of notochordal NP cells in 10-year-old humans is responsible for the degeneration of the IVD with aging, the fact that the IVD is free of degeneration well into late middle age suggests that chondrocyte-like NP cells alone enable NP function for a prolonged time. This suggestion is consistent with our results that hiPS-Cart implanted into the nuclectomized space prevented IVD degeneration, implying that notochordal NP cells are dispensable for NP function. Nevertheless, it is likely that notochordal NP cells play important roles in the induction and maturation of chondrocyte-like
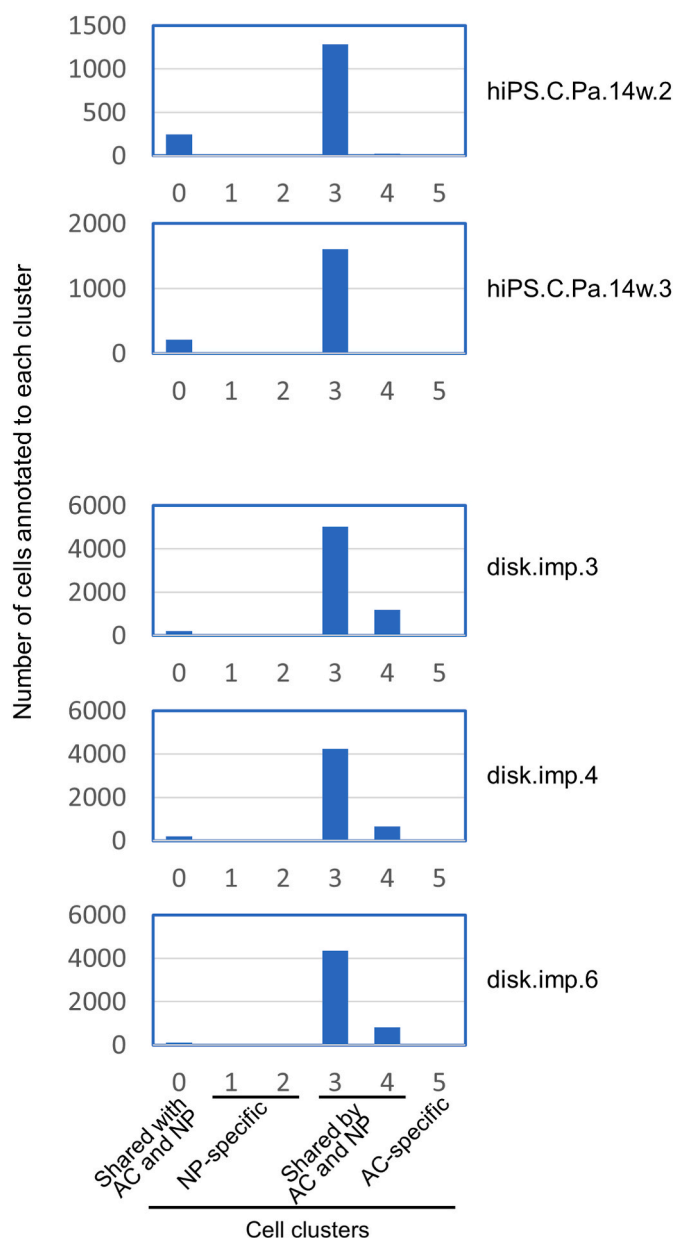
Fig. 7. Annotation of hiPS-Cart cells before and after implantation against NP cell clusters using SingleR. We annotated hiPS-Cart cells before and after implantation against the six cell clusters defined in NP cells (Fig. 6B) as a reference using SingleR. The number of cells that were annotated to each cluster were calculated using SingleR functions and plotted.

cells in NP during development. Notochord-like cells have been successfully induced from ESCs and iPSCs by directed differentiation that mimics the developmental process of notochord [50–53]. Furthermore, the implantation of iPSC-derived notochord-like cells into a rat injury model moderately rescued disk height [52]. Notochord-like cells, when implanted into injured sites, may powerfully induce NP tissue by stimulating surviving host NP cells, including progenitor cells, to differentiate into chondrocyte-like cells.

Many cell therapies against NP lesions act through trophic effects, in which the implanted cells reside only transiently and secrete factors that stimulate host resident progenitor cells to repair the tissue [54]. Because the regenerative potential of resident cells is limited, the repaired tissue shows inferior NP function compared with undamaged NP. While regular cell implantation likely results in transient cell survival, long-term survival can be achieved when cells are implanted as a

tissue-engineered construct wherein the cells are embedded in a scaffold, such as a hydrogel [55–57] and a fibrin carrier [58]. The scaffold should contribute to cell survival and tissue healing through its mechanical properties. In this study, we developed a human iPS cell-derived cartilage (hiPS-Cart) that is a scaffoldless cartilaginous tissue, *in vitro*. hiPS-Cart consists of hiPSC-derived chondrocytes and ECM that the hiPSC-derived chondrocytes produced in three-dimensional culture. The ECM contributes to cell survival and tissue healing through its mechanical properties and by providing a favorable environment for differentiation of the cells after hiPS-Cart implantation. We found that hiPS-Cart survived and directly replaced NP spatially and functionally in rats for at least 6 months after implantation into IVD. Notably, this healing mechanism does not rely on the regenerative potential of host resident cells, suggesting a more stable clinical outcome even when host progenitor cells are completely lost.

Limitations of this study include the use of small animals (rats) for the animal experiments and the observation period of up to 6 months. A large animal model and longer observation period are needed to confirm that hiPS-Cart can replace NP. We compared monkey NP scRNA-seq data with that of hiPS-Cart because it was difficult for us to obtain human NP samples, especially from donors under 10 years old who have notochordal NP cells. Therefore, we should be cautious in interpreting the data, because human and monkey may have different markers. The differentiation methods to create hiPS-Cart from hiPSCs *in vitro* can be further refined for ideal NP constructs in the future. For example, a co-culture with notochordal NP cells, including hiPSC-derived notochordal NP cells, may contribute to the production of higher quality hiPS-Cart *in vitro* for the purpose of NP regeneration. scRNA-seq data of NP will provide new information on the signals inducing NP cells, thus contributing to the development of a differentiation protocol for hiPSC-derived NP. While safety issues such as the tumorigenicity of implanted hiPS-Cart into knee joints have been analyzed [17,59], these issues for hiPS-Cart implanted into spine have not. Overall, further studies are needed before clinical translation, but our results suggest that hiPS-Cart is a candidate construct for the regeneration of NP to treat IVD degeneration.

5. Conclusion

hiPS-Cart is scaffoldless cartilaginous tissue created from hiPSCs. scRNA-seq analysis revealed that the cells in hiPS-Cart correspond to middle/deep zone chondrocytes in AC as well as chondrocyte-like NP cells. hiPS-Cart implanted into the nuclectomized space survived and prevented IVD degeneration, indicating that hiPS-Cart spatially and functionally replaces NP. Therefore, hiPS-Cart is a candidate implant for regenerating NP spatially and functionally and preventing IVD degeneration.
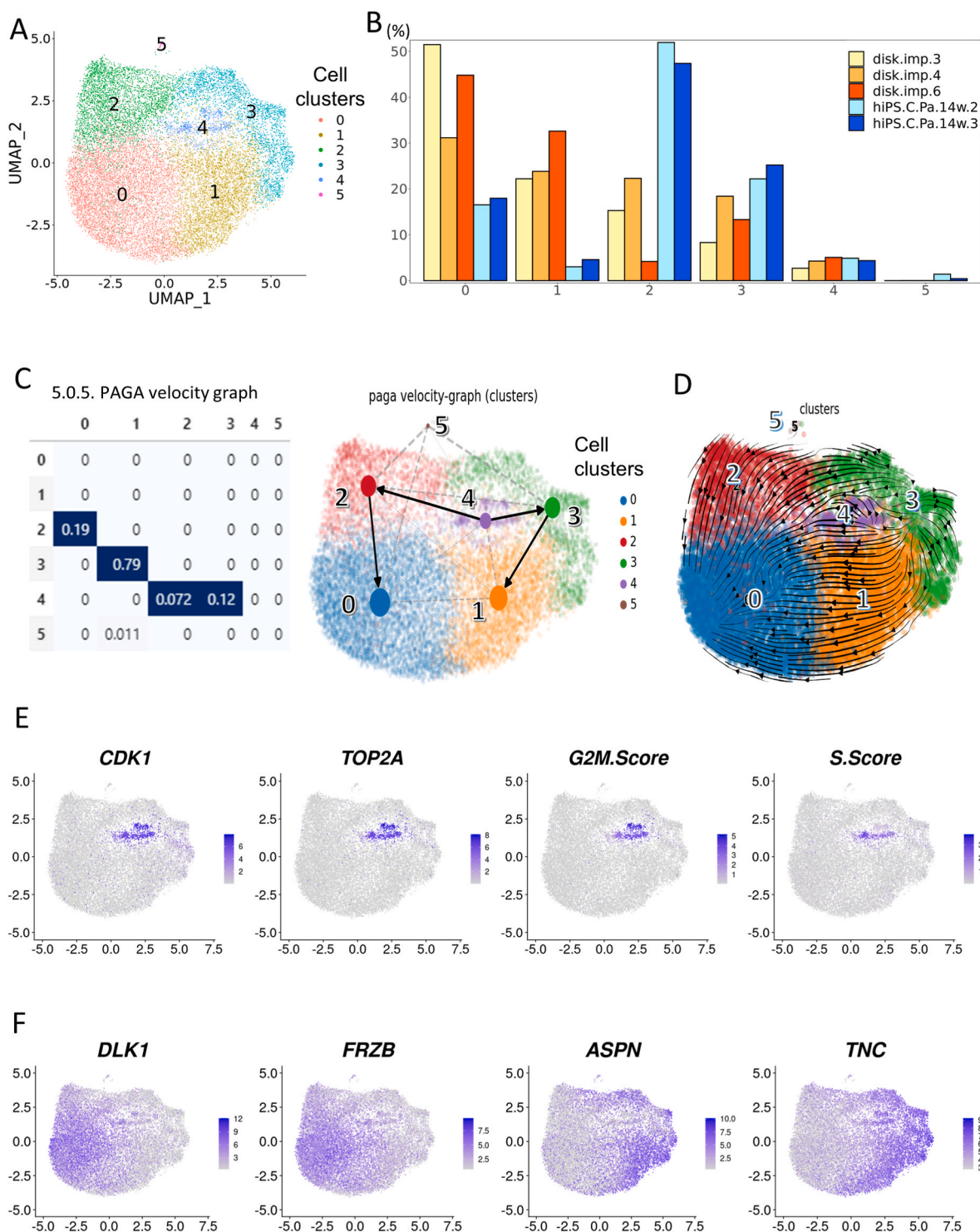
Fig. 8. Differentiation of hiPS-Cart cells after implantation. A) Pre-implant and post-implant hiPS-Cart cells were used to generate UMAP plots with the resolution parameter = 0.25. Cells were separated into six clusters. B) The ratio of cells in each cell cluster in each sample are plotted. C, D) Post-implant hiPS-Cart cells were subjected to RNA velocity analysis using scVelo. The trajectory inference using PAGA[37] extended by the velocity-inferred directionality (C). We ran the dynamical model of scVelo, and velocity vectors were projected on the UMAP plot using the scv.pl.velocity_embedding_stream function (D). E) Expression levels of DEGs found in cluster #4 (*CDK1* and *TOP2A*) and G2M.Score and S.Score are indicated for each cell in pre-implant and post-implant hiPS-Cart projected on the UMAP plot using the FeaturePlot function. F) Expression levels of DEGs found in cluster #0 (*DLK1* and *FRZB*) and cluster #1 (*ASPN* and *TNC*) are indicated for each cell in pre-implant and post-implant hiPS-Cart projected on the UMAP plot using the FeaturePlot function.

Data availability

All original data are available upon request to the authors. Our scRNA-seq datasets are available on GEO accession number GSE197380.

Credit author statement

Takashi Kamatani: Designing the experiments, Implanted the hiPS-Cart into rats, X-ray, micro-CT, and histology analysis, Writing manuscript. Hiroki Hagizawa: Designing the experiments, Implanted the hiPS-Cart into rats, X-ray, micro-CT, and histology analysis, scRNA-seq analysis, Writing manuscript. Seido Yarimitsu: Biomechanical test, scRNA-seq analysis. Miho Morioka: Creation of hiPS-Cart. Saeko Koyamatsu: scRNA-seq analysis. Michihiko Sugimoto: scRNA-seq analysis. Joe Kodama: Implanted the hiPS-Cart into rats. Junko Yamane: scRNA-seq analysis. Hiroyuki Ishiguro: Implanted the hiPS-Cart into rats. Shigeyuki Shichino: scRNA-seq analysis. Kuniya Abe: scRNA-seq analysis. Wataru Fujibuchi: scRNA-seq analysis. Hiromichi Fujie: Biomechanical test. Takashi Kaito: Designing the experiments, Implanted the hiPS-Cart into rats, Writing manuscript, Conceiving the study. Noriyuki Tsumaki: Designing the experiments, scRNA-seq analysis, Writing manuscript, Conceiving the study.

Declaration of competing interest

The authors declare that they have no known competing financial interests or personal relationships that could have appeared to influence the work reported in this paper.

Appendix A. Supplementary data

Supplementary data to this article can be found online at https://doi.org/10.1016/j.biomaterials.2022.121491.

References

[1] T. Vos, A.D. Flaxman, M. Naghavi, R. Lozano, C. Michaud, M. Ezzati, .Z.A. Memish, Years lived with disability (YLDs) for 1160 sequelae of 289 diseases and injuries 1990-2010: a systematic analysis for the Global Burden of Disease Study 2010, Lancet 380 (9859) (2012) 2163–2196.

[2] R.D. Meucci, A.G. Fassa, N.M. Faria, Prevalence of chronic low back pain: systematic review, Rev. Saude Publica 49 (2015) 1.

[3] M.J. DePalma, J.M. Ketchum, T. Saullo, What is the source of chronic low back pain and does age play a role? Pain Med. 12 (2) (2011) 224–233.

[4] P. Verrills, G. Nowesenitz, A. Barnard, Prevalence and characteristics of discogenic pain in tertiary practice: 223 consecutive cases utilizing lumbar discography, Pain Med. 16 (8) (2015) 1490–1499.

[5] D. Hoy, L. March, P. Brooks, F. Blyth, A. Woolf, C. Bain, .R. Buchbinder, The global burden of low back pain: estimates from the Global Burden of Disease 2010 study, Ann. Rheum. Dis. 73 (6) (2014) 968–974.

[6] J.N. Katz, Lumbar disc disorders and low-back pain: socioeconomic factors and consequences, J. Bone Joint Surg. Am. 88 (Suppl 2) (2006) 21–24.

[7] D. Sakai, Future perspectives of cell-based therapy for intervertebral disc disease, Eur. Spine J. 17 (Suppl 4) (2008) 452–458.

[8] P. Park, H.J. Garton, V.C. Gala, J.T. Hoff, J.E. McGillicuddy, Adjacent segment disease after lumbar or lumbosacral fusion: review of the literature, Spine 29 (17) (2004) 1938–1944.

[9] K.J. Cho, S.I. Suk, S.R. Park, J.H. Kim, S.S. Kim, W.K. Choi, .S.R. Lee, Complications in posterior fusion and instrumentation for degenerative lumbar scoliosis, Spine 32 (20) (2007) 2232–2237.

[10] J. Antoniou, T. Steffen, F. Nelson, N. Winterbottom, A.P. Hollander, R.A. Poole, . M. Alini, The human lumbar intervertebral disc: evidence for changes in the biosynthesis and denaturation of the extracellular matrix with growth, maturation, ageing, and degeneration, J. Clin. Invest. 98 (4) (1996) 996–1003.

[11] D.M. O'Halloran, A.S. Pandit, Tissue-engineering approach to regenerating the intervertebral disc, Tissue Eng. 13 (8) (2007) 1927–1954.

[12] T.C. Schmitz, E. Salzer, J.F. Crispim, G.T. Fabra, C. LeVisage, A. Pandit, .K. Ito, Characterization of biomaterials intended for use in the nucleus pulposus of degenerated intervertebral discs, Acta Biomater. 114 (2020) 1–15.

[13] J.A. Waxenbaum, V. Reddy, B. Futterman, Anatomy, Back, Intervertebral Discs, StatPearls, StatPearls Publishing Copyright © 2021, StatPearls Publishing LLC., Treasure Island (FL), 2021.

[14] D. Nedresky, V. Reddy, G. Singh, Anatomy, Back, Nucleus Pulposus, StatPearls, StatPearls Publishing Copyright © 2021, StatPearls Publishing LLC., Treasure Island (FL), 2021.

[15] K. Takahashi, K. Tanabe, M. Ohnuki, M. Narita, T. Ichisaka, K. Tomoda, S. Yamanaka, Induction of pluripotent stem cells from adult human fibroblasts by defined factors, Cell 131 (5) (2007) 861–872.

[16] R. Castro-Vinuelas, C. Sanjurjo-Rodriguez, M. Pineiro-Ramil, T. Hermida-Gomez, I. M. Fuentes-Boquete, F.J. de Toro-Santos, .S.M. Diaz-Prado, Induced pluripotent stem cells for cartilage repair: current status and future perspectives, Eur. Cell. Mater. 36 (2018) 96–109.

[17] A. Yamashita, M. Morioka, Y. Yahara, M. Okada, T. Kobayashi, S. Kuriyama, . N. Tsumaki, Generation of scaffoldless hyaline cartilaginous tissue from human iPSCs, Stem Cell Rep. 4 (3) (2015) 404–418.

[18] A. Yamashita, N. Tsumaki, Recent progress of animal transplantation studies for treating articular cartilage damage using pluripotent stem cells, Dev. Growth Differ. 63 (1) (2021) 72–81.

[19] J.J. Trout, J.A. Buckwalter, K.C. Moore, Ultrastructure of the human intervertebral disc: II. Cells of the nucleus pulposus, Anat. Rec. 204 (4) (1982) 307–314.

[20] S. Tessier, M.V. Risbud, Understanding embryonic development for cell-based therapies of intervertebral disc degeneration: toward an effort to treat disc degeneration subphenotypes, Dev. Dynam. 250 (3) (2021) 302–317.

[21] B.M. Minogue, S.M. Richardson, L.A. Zeef, A.J. Freemont, J.A. Hoyland, Transcriptional profiling of bovine intervertebral disc cells: implications for identification of normal and degenerate human intervertebral disc cell phenotypes, Arthritis Res. Ther. 12 (1) (2010) R22.

[22] V. Tam, P. Chen, A. Yee, N. Solis, T. Klein, M. Kudelko, .D. Chan, DIPPER, a spatiotemporal proteomics atlas of human intervertebral discs for exploring ageing and degeneration dynamics, Elife 9 (2020).

[23] K. Okita, Y. Matsumura, Y. Sato, A. Okada, A. Morizane, S. Okamoto, . S. Yamanaka, A more efficient method to generate integration-free human iPS cells, Nat. Methods 8 (5) (2011) 409–412.

[24] A. Yamashita, H. Yoshitomi, S. Kihara, J. Toguchida, N. Tsumaki, Culture Substrate-Associated YAP Inactivation Underlies Chondrogenic Differentiation of Human Induced Pluripotent Stem Cells, Stem Cells Translational Medicine, 2020.

[25] S. Shichino, S. Ueha, S. Hashimoto, T. Ogawa, H. Aoki, .K. Matsushima, TAS-seq: a Robust and Sensitive Amplification Method for Beads-Based scRNA-Seq, 2021 bioRxiv.

[26] A.D. Yates, P. Achuthan, W. Akanni, J. Allen, J. Allen, J. Alvarez-Jarreta, .P. Flicek, Ensembl 2020, Nucleic Acids Res. 48 (D1) (2020) D682–D688.

[27] A.T.L. Lun, S. Riesenfeld, T. Andrews, T.P. Dao, T. Gomes, J. participants in the 1st Human Cell Atlas, J.C. Marioni, EmptyDrops: distinguishing cells from empty droplets in droplet-based single-cell RNA sequencing data, Genome Biol. 20 (1) (2019) 63.

[28] M.-P.J. Finak G, R. Gottardo, flowTrans: Parameter Optimization for Flow Cytometry Data Transformation, 2019. R package version 1.36.0.

[29] L. Scrucca, M. Fop, T.B. Murphy, A.E. Raftery, Mclust 5: clustering, classification and density estimation using Gaussian finite mixture models, R J 8 (1) (2016) 289–317.

[30] Y. Hao, S. Hao, E. Andersen-Nissen, W.M. Mauck III, S. Zheng, A. Butler, .R. Satija, Integrated analysis of multimodal single-cell data, Cell 184 (13) (2021) 3573–3587, e29.

[31] Single-cell transcriptomics of 20 mouse organs creates a Tabula Muris, Nature 562 (7727) (2018) 367–372.

[32] D. Aran, A.P. Looney, L. Liu, E. Wu, V. Fong, A. Hsu, .M. Bhattacharya, Reference-based analysis of lung single-cell sequencing reveals a transitional profibrotic macrophage, Nat. Immunol. 20 (2) (2019) 163–172.

[33] D. Kim, J.M. Paggi, C. Park, C. Bennett, S.L. Salzberg, Graph-based genome alignment and genotyping with HISAT2 and HISAT-genotype, Nat. Biotechnol. 37 (8) (2019) 907–915.

[34] Y. Liao, G.K. Smyth, W. Shi, featureCounts: an efficient general purpose program for assigning sequence reads to genomic features, Bioinformatics 30 (7) (2014) 923–930.

[35] G. La Manno, R. Soldatov, A. Zeisel, E. Braun, H. Hochgerner, V. Petukhov, .P. V. Kharchenko, RNA velocity of single cells, Nature 560 (7719) (2018) 494–498.

[36] V. Bergen, M. Lange, S. Peidli, F.A. Wolf, F.J. Theis, Generalizing RNA velocity to transient cell states through dynamical modeling, Nat. Biotechnol. 38 (12) (2020) 1408–1414.

[37] F.A. Wolf, F.K. Hamey, M. Plass, J. Solana, J.S. Dahlin, B. Göttgens, .F.J. Theis, PAGA: graph abstraction reconciles clustering with trajectory inference through a topology preserving map of single cells, Genome Biol. 20 (1) (2019) 59.

[38] K. Masuda, Y. Aota, C. Muehleman, Y. Imai, M. Okuma, E.J. Thonar, .H.S. An, A novel rabbit model of mild, reproducible disc degeneration by an anulus needle puncture: correlation between the degree of disc injury and radiological and histological appearances of disc degeneration, Spine 30 (1) (2005) 5–14.

[39] H. Ishiguro, T. Kaito, S. Yarimitsu, K. Hashimoto, R. Okada, J. Kushioka, . H. Yoshikawa, Intervertebral disc regeneration with an adipose mesenchymal stem cell-derived tissue-engineered construct in a rat nucleotomy model, Acta Biomater. 87 (2019) 118–129.

[40] C.R. Flannery, C.E. Hughes, B.L. Schumacher, D. Tudor, M.B. Aydelotte, K. E. Kuettner, B. Caterson, Articular cartilage superficial zone protein (SZP) is homologous to megakaryocyte stimulating factor precursor and Is a multifunctional proteoglycan with potential growth-promoting, cytoprotective, and lubricating properties in cartilage metabolism, Biochem. Biophys. Res. Commun. 254 (3) (1999) 535–541.

[41] S.H. Peck, K.K. McKee, J.W. Tobias, N.R. Malhotra, B.D. Harfe, L.J. Smith, Whole transcriptome analysis of notochord-derived cells during embryonic formation of the nucleus pulposus, Sci. Rep. 7 (1) (2017) 10504.

[42] S.M. Richardson, F.E. Ludwinski, K.K. Gnanalingham, R.A. Atkinson, A.J. Freemont, J.A. Hoyland, Notochordal and nucleus pulposus marker expression is maintained by sub-populations of adult human nucleus pulposus cells through aging and degeneration, Sci. Rep. 7 (1) (2017) 1501.

[43] J.J. Trout, J.A. Buckwalter, K.C. Moore, S.K. Landas, Ultrastructure of the human intervertebral disc. I. Changes in notochordal cells with age, Tissue Cell 14 (2) (1982) 359–369.

[44] L.M. Fernandes, N.M. Khan, C.M. Trochez, M. Duan, M.E. Diaz-Hernandez, S.M. Presciutti, .H. Drissi, Single-cell RNA-seq identifies unique transcriptional landscapes of human nucleus pulposus and annulus fibrosus cells, Sci. Rep. 10 (1) (2020).

[45] Y. Zhang, S. Han, M. Kong, Q. Tu, L. Zhang, X. Ma, Single-cell RNA-Seq Analysis Identifies Unique Chondrocyte Subsets and Reveals Involvement of Ferroptosis in Human Intervertebral Disc Degeneration, Osteoarthritis Cartilage, 2021.

[46] V. Madhu, P.K. Boneski, E. Silagi, Y. Qiu, I. Kurland, A.R. Guntur, .M.V. Risbud, Hypoxic regulation of mitochondrial metabolism and mitophagy in nucleus pulposus cells is dependent on HIF-1α-BNIP3 Axis, J. Bone Miner. Res. 35 (8) (2020) 1504–1524.

[47] T.E. O'Sullivan, L.R. Johnson, H.H. Kang, J.C. Sun, BNIP3- and BNIP3L-mediated mitophagy promotes the generation of natural killer cell memory, Immunity 43 (2) (2015) 331–342.

[48] M.R. McCann, O.J. Tamplin, J. Rossant, C.A. Séguin, Tracing notochord-derived cells using a Noto-cre mouse: implications for intervertebral disc development, Dis. Model Mech. 5 (1) (2012) 73–82.

[49] K.S. Choi, M.J. Cohn, B.D. Harfe, Identification of nucleus pulposus precursor cells and notochordal remnants in the mouse: implications for disk degeneration and chordoma formation, Dev. Dynam. 237 (12) (2008) 3953–3958.

[50] M.K. Winzi, P. Hyttel, J.K. Dale, P. Serup, Isolation and characterization of node/notochord-like cells from mouse embryonic stem cells, Stem Cell. Dev. 20 (11) (2011) 1817–1827.

[51] M.E. Diaz-Hernandez, N.M. Khan, C.M. Trochez, T. Yoon, P. Maye, S.M. Presciutti, H. Drissi, Derivation of notochordal cells from human embryonic stem cells reveals unique regulatory networks by single cell-transcriptomics, J. Cell. Physiol. 235 (6) (2020) 5241–5255.

[52] Y. Zhang, Z. Zhang, P. Chen, C.Y. Ma, C. Li, T.Y.K. Au, Q. Lian, Directed differentiation of notochord-like and nucleus pulposus-like cells using human pluripotent stem cells, Cell Rep. 30 (8) (2020) 2791–2806, e5.

[53] K. Xia, J. Zhu, J. Hua, Z. Gong, C. Yu, X. Zhou, C. Liang, Intradiscal injection of induced pluripotent stem cell-derived nucleus pulposus-like cell-seeded polymeric microspheres promotes rat disc regeneration, Stem Cell. Int. 2019 (2019) 6806540.

[54] G. Vadala, L. Ambrosio, F. Russo, R. Papalia, V. Denaro, Interaction between mesenchymal stem cells and intervertebral disc microenvironment: from cell therapy to tissue engineering, Stem Cell. Int. 2019 (2019) 2376172.

[55] H.B. Henriksson, T. Svanvik, M. Jonsson, M. Hagman, M. Horn, A. Lindahl, H. Brisby, Transplantation of human mesenchymal stems cells into intervertebral discs in a xenogeneic porcine model, Spine 34 (2) (2009) 141–148.

[56] Y. Gan, P. Li, L. Wang, X. Mo, L. Song, Y. Xu, Q. Zhou, An interpenetrating network-strengthened and toughened hydrogel that supports cell-based nucleus pulposus regeneration, Biomaterials 136 (2017) 12–28.

[57] D. Sheyn, S. Ben-David, W. Tawackoli, Z. Zhou, K. Salehi, M. Bez, Z. Gazit, Human iPSCs can be differentiated into notochordal cells that reduce intervertebral disc degeneration in a porcine model, Theranostics 9 (25) (2019) 7506–7524.

[58] F.L. Acosta Jr., L. Metz, H.D. Adkisson, J. Liu, E. Carruthers-Liebenberg, C. Milliman, J.C. Lotz, Porcine intervertebral disc repair using allogeneic juvenile articular chondrocytes or mesenchymal stem cells, Tissue Eng. Part A 17 (23–24) (2011) 3045–3055.

[59] Y. Takei, M. Morioka, A. Yamashita, T. Kobayashi, N. Shima, N. Tsumaki, Quality assessment tests for tumorigenicity of human iPS cell-derived cartilage, Sci. Rep. 10 (1) (2020) 12794.